Chapter 1
Solid-State Nanopore Sensors for Nucleic Acid Analysis

Bala Murali Venkatesan and Rashid Bashir

Abstract Solid-state nanopores are *nm* sized apertures formed in thin synthetic membranes. These single molecule sensors have been used in a variety of biophysical and diagnostic applications and serve as a potential candidate in the development of cost-effective, next generation DNA sequencing technologies, critical to furthering our understanding of inheritance, individuality, disease and evolution. The versatility of solid-state nanopore technology allows for both interfacing with biological systems at the nano-scale as well as large scale VLSI integration promising reliable, affordable, mass producible biosensors with single molecule sensing capabilities. In addition, this technology allows for truly parallel, high throughput DNA and protein analysis through the development of nanopore and micropore arrays in ultra-thin synthetic membranes. This chapter is focused on the development of solid-state nanopore sensors in synthetic membranes and the potential benefits and challenges associated with this technology. Biological nanopores, primarily *α-hemolysin* and the *phi29* connector are also reviewed. We conclude with a detailed discussion on chemically modified solid-state nanopores. These surface functionalized nanopore sensors combine the stability and versatility of solid-state nanopores with the sensitivity and selectivity of biological nanopore systems and may play an important role in drug screening and medical diagnostics.

B.M. Venkatesan (✉)
Department of Electrical and Computer Engineering, Micro and Nanotechnology Lab, University of Illinois at Urbana-Champaign, Champaign, IL 61820, USA
e-mail: bvenkate@illinois.edu

R. Bashir (✉)
Department of Electrical and Computer Engineering, Department of Bioengineering, Micro and Nanotechnology Lab, University of Illinois at Urbana-Champaign, Champaign, IL 61820, USA
e-mail: rbashir@illinois.edu

S.M. Iqbal and R. Bashir (eds.), *Nanopores: Sensing and Fundamental Biological Interactions*, DOI 10.1007/978-1-4419-8252-0_1,

Keywords α-hemolysin • phi29 • Nanopores in Al_2O_3 Membranes • Surface Charges in Nanopores • Surface Enhanced DNA Transport

1.1 Introduction

Our quest to better understand the origins of inheritance, individuality, disease and evolution has led to some of the greatest scientific and technological discoveries in history. This journey has taken us from the macro-scale world that we live in, to the micro-scale environments in which cells and bacteria operate, down to the nano-scale in which single molecules of DNA, RNA and proteins exist. The discovery of microorganisms in the late 1600s by Anton Van Leeuwenhoek laid the foundation for modern microbiology and bacteriology, making possible the discovery of processes such as cell division and cell differentiation. Gregor Mendel's discovery of the laws of inheritance through observations involving the physical traits passed on between generations of pea plants, laid the foundation for modern day genetics. Latter work by Oswald Avery confirmed that this genetic information is carried by deoxyribonucleic acid or DNA.

The discovery of DNA as the blue prints of life in all living organisms is of fundamental importance in medicine and biology. DNA contains the instruction set that is used to encode RNA and proteins, the machinery that drives all cellular activity. Chemically, DNA consists of two long polymers composed of simple sub-units called nucleotides arranged in a double helix structure. Each nucleotide contains a sugar-phosphate backbone attached to one of four types of molecules called bases, specifically Adenine, Thymine, Cytosine and Guanine. It is the sequence of these four bases along the DNA backbone that encodes the genetic information that defines the various characteristics of an organism. Due to the vast information content of DNA and its importance in regulating cellular behavior, widespread research is focused on the development of technologies applicable to DNA analysis.

Gel electrophoresis is the most commonly used tool in DNA analysis and is the work-horse of conventional DNA Sanger sequencing platforms [73]. In gel electrophoresis, charged biopolymers are electrically driven through a 'gel', consisting of a heterogeneous, three-dimensional matrix of pores ranging in diameter from a few nanometers up to hundreds of nanometers. The gel is composed of either polyacrylamide or agarose depending on the specific weight and composition of the analyte of interest. Electrophoresis of DNA is made possible by the charged nature of this polymer in solution. The isoelectric point of the phosphate group on the DNA backbone is ~1 resulting in a single negative charge per nucleotide under most experimental conditions, including physiological pH. In solution, this charge is partially shielded due to counterion condensation according to Manning theory [57]. During gel electrophoresis, strong interactions between DNA and the pore network result in the fine separation of even relatively similar molecular

species, based on the enhanced mobility of shorter molecules in the gel. This technique finds application in DNA and protein purification, DNA length separation assays and in DNA sequencing [9]. The limitation of this technique however, is that it involves the simultaneous processing of millions or billions of molecules in order to provide a macroscale optical readout. This in turn translates to large analyte volumes, increased preparation time and high cost. In addition, the output is averaged over a population of molecules and is less sensitive to subtle structural variations amongst molecules. Single molecule sensing methods could help overcome these limitations. Single molecule sensing methods employ highly sensitive optical and electrical technologies to interrogate and analyze individual molecules thereby reducing required analyte volumes and cost. One such technology that finds application in single molecule DNA analysis with potential application to next generation DNA sequencing, is the use of nanopores.

Nanopores are *nm* sized apertures embedded in biological membranes or fabricated in solid-state membranes. Though the passage of biomolecules and ions through nanopores is commonplace in biology, it is only recently that researchers have been able to successfully drive single biomolecules such as DNA through proteinaceous and solid-state nanopores in-vitro [22, 43]. Solid-state nanopore platforms are capable of resistively sensing individual biomolecules including DNA, RNA and small proteins. The concept of resistive particle sensing in solutions was first pioneered by Coulter in the early 1950s [21]. This work led to the development of the Coulter Counter, now a commonly used device for obtaining complete blood cell counts. The principle governing the operation of the Coulter counter is relatively simple. An aperture, slightly larger than the analyte of interest separates two chambers filled with conductive electrolyte. Electrodes immersed in each chamber are used to apply an electric potential, creating a current of ions through the aperture. As the analyte of interest passes through the aperture, the ionic current is partially blocked and this perturbation is sensed electrically revealing useful information about the particle.

Nanopore based single molecule sensors use this exact same principle, only at the nano-scale where the size of this aperture is comparable to the 2.2 nm cross sectional diameter of an individual dsDNA molecule. Briefly, a silicon support containing a single nanopore of diameter comparable to the diameter of an individual DNA molecule is fabricated (Fig. 1.1a) and then inserted into a flow cell containing two chambers filled with conductive electrolyte (Fig. 1.1b). An electrode is immersed in each chamber as shown, and a potential is applied across the nanopore chip, resulting in an ionic current through the pore corresponding to the open pore current. Target DNA molecules are next inserted into the *cis* chamber of the fluidic setup. Two-terminal electrophoresis is used to drive the negatively charged DNA molecule through the nanopore (Fig. 1.1c), resulting in transient current blockades as seen in Fig. 1.1d. These electrical signatures are then analyzed, revealing useful information about the translocating molecule [89, 90]. This technique has been used to study various biophysical phenomena at the single molecule level including the label-free

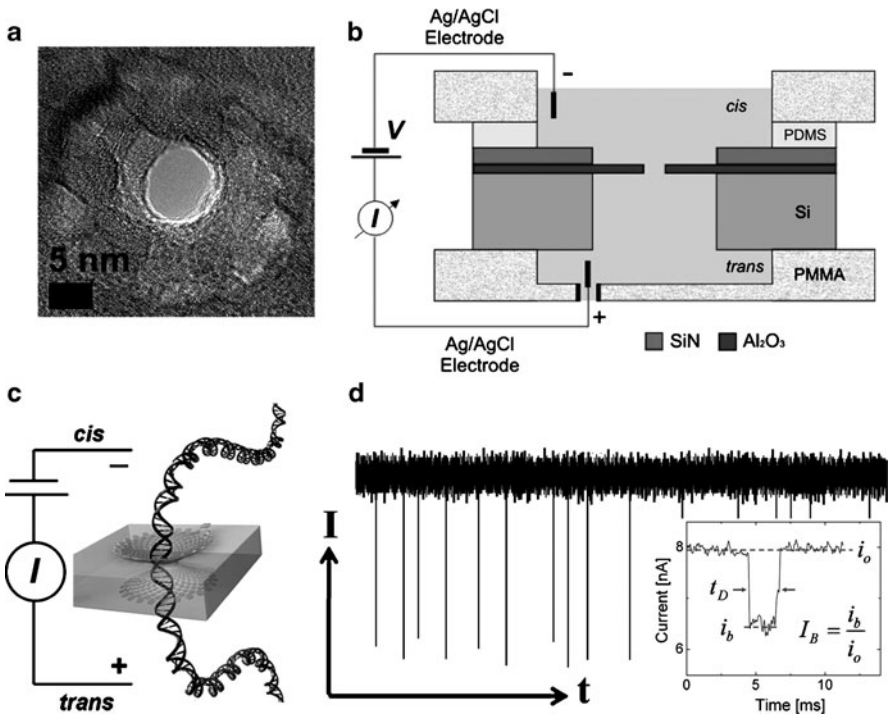

Fig. 1.1 (**a**) Transmission Electron Microscope (TEM) image of a 7 nm Al_2O_3 nanopore (**b**) Nanopore fluidic setup showing Si nanopore chip encapsulated between two chambers of a PMMA flow cell filled with conductive electrolyte (**c**) Schematic of DNA transport through a nanopore (**d**) Characteristic downward current blockades seen during the transport of individual DNA molecules through the pore (Inset) Current signature corresponding to a single DNA translocation event showing, blockage ratio I_B, and translocation time, t_D, specific to the translocation event

detection of single nucleotide polymorphisms (SNP's) with application to cancer diagnostics [36], stretching transitions in individual dsDNA [31], unzipping kinetics of hairpin DNA molecules [59], DNA sizing and sieving [85], and the detection of DNA-protein complexes essential in DNA repair [80].

1.2 Nanopores in Biology

The biological cell contains various types of nanopores and nanochannels that regulate the flow of ions and molecules into and out of the cell. These nanopores play a vital role in cellular processes such as intercellular communication and signaling between subcellular structures. Examples include gated, selective ion channels that connect the cell cytosol to the cell exterior; nuclear membrane pores that control the passage of biomolecules such as messenger RNA (mRNA) from the cell nucleus into the cytosol; proteins that are secreted across pores in the

membranes of cell organelles; and viruses, which dump their genomes into cells via pores that insert into the cell membrane [22]. An example of a biological nanopore that is frequently used in-vitro is the α-*hemolysin* channel.

1.2.1 α-Hemolysin

α-*hemolysin* is a naturally occurring biological protein complex extracted from the bacterium *Staphylococcus aureus* that when inserted into a lipid bilayer membrane, forms a ~1.5 nm diameter pore allowing the passage of ions and ssDNA. In vivo, bacterium *Staphylococcus aureus* secretes alpha-hemolysin monomers that bind to the outer membrane of host cells. These monomers self assemble into seven subunit oligomers to form a water-filled transmembrane channel that facilitates the uncontrolled permeation of water, ions, and small organic molecules in and out of the host cell. The resulting discharge of vital molecules from the host cell, osmotic swelling and a loss in ionic gradient can result in irreversible cell damage and eventually death of the host cell (apoptosis). Apoptosis induced by α-*hemolysin* insertion in various cell types including rabbit erythrocytes, human erythrocytes, monocytes, and lymphocytes has been reported [4, 40].

In-vitro studies of DNA transport through biological pores have traditionally focused on α-*hemolysin* as the transmembrane channel of choice. The structure of the heptameric α-*hemolysin* pore embedded in a lipid bilayer is shown in Fig. 1.2a.

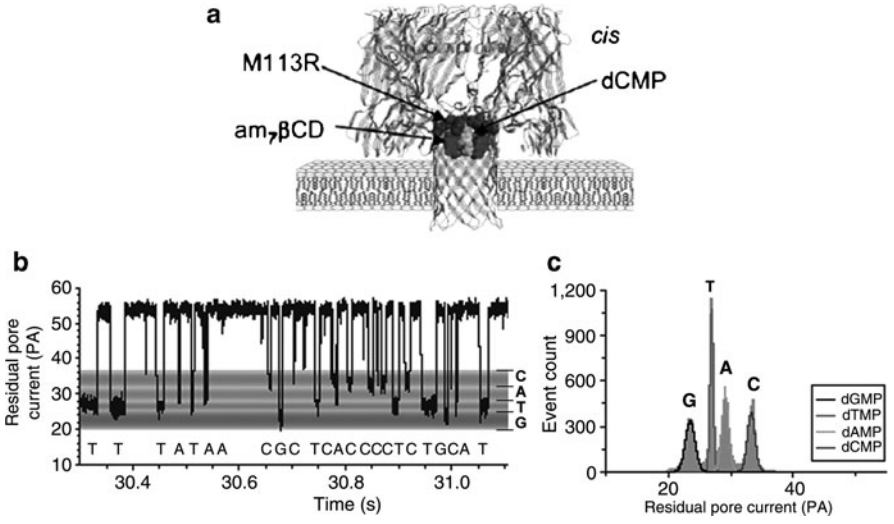

Fig. 1.2 Single nucleotide detection using a mutant α-*hemolysin* nanopore [18], reprinted with permission. (**a**) Mutant α-*hemolysin* protein channel modified with a cyclodextrin adapter embedded in a lipid bilayer (**b**) Characteristic current recordings from a modified α-*hemolysin* channel, showing different blockade levels for each base (**c**) Current blockade histogram confirms single base discrimination ability of modified α-*hemolysin* pore

The total channel length is 10 nm and is comprised of a 5 nm vestibule that protrudes into the *cis* compartment and a 5 nm transmembrane domain embedded in the lipid bilayer. Between pH 7–9, α-*hemolysin* forms a relatively stable and reproducible non-gating channel with less than 2% variation in open pore current under temperature stabilized conditions [96]. The comparable inner channel diameter of α-*hemolysin* to ssDNA (diameter ~1.3 nm) suggests that less than one Debye length (~3 Å in 1 M KCl) separates the translocating biomolecule from the amino acid residues in the pore. Although dsDNA is too large to translocate through α-*hemolysin*, up to a 10 bp fragment can reside in the vestibule. This makes α-*hemolysin* a very powerful tool for examining biomolecular interactions and the binding affinities of individual molecules at the single molecule level.

In a landmark study, Kasianowicz et al. demonstrated the ability to electrically detect individual ssDNA and ssRNA molecules using α-*hemolysin* nanopores embedded in planar phospholipid bilayers [43]. A plethora of studies have since followed elucidating the biophysics of single molecule transport through proteinaceous α-*hemolysin*. For example, Meller et al. examined the effects of polymer length on translocation velocity [61]. Polymers longer than the pore length were seen to translocate at constant speed however shorter polymers exhibited a length dependent velocity. Studies by Mathe et al. revealed that α-*hemolysin* nanopore sensors are sensitive enough to differentiate between 3′ and 5′ threading of ssDNA in the pore with 5′ threading resulting in a twofold increase in translocation times relative to 3′ threading, attributed to the tilt reorientation of bases towards the 5′ end of the molecule [58]. Brun et al. showed that biomolecule flux through proteinaceous α-*hemolysin* is highly dependent on the applied voltage with the capture rate of ssDNA [60, 64] and small polyelectrolytes [8], following a simple Van't Hoff-Arrhenius relationship. Kasianowicz and co-workers further showed that the asymmetric structure of α-*hemolysin* promotes biomolecule entry from the *cis* side (side with the vestibule) as opposed to the *trans* side [32]. Reduced biomolecule flux from the *trans* side was attributed to a combination of factors; (1) the high entropic barrier associated with the highly confined geometry of the β barrel on the *trans* side and (2) electrostatic repulsion of DNA by the negatively charged asparatic acid residues located on the *trans* side. The unzipping of hair-pin DNA structures using α-*hemolysin* was observed by Vercoutere et al. for sufficiently short hairpins. Vercoutere demonstrated the ability to discriminate between 3 and 8 bp long hairpins with single base resolution [92]. Meller further demonstrated that sequence specific information could be derived directly from ssDNA translocation experiments through biological α-*hemolysin* [60]. Poly(dA) and Poly(dC) strands exhibited different translocation times attributed to the strong base stacking of poly(dA) relative to poly(dC), thereby making the poly(dA) sequence more rigid during translocation.

α-*hemolysin* nanopores also hold tremendous value in the field of DNA sequencing. Stoddart recently demonstrated the ability to resolve individual nucleotides located in homopolymeric and heteropolymeric ssDNA immobilized in biological α-*hemolysin* [83]. Mitchell et al. showed that chemical labels attached to bases could be used to resolve individual bases in a translocating DNA strand [62]. Interestingly blockage durations and amplitudes could be tuned by varying the

chemistry, charge and size of these chemical tags, suggesting the possibility of base discrimination based on peptide labeling with application to DNA sequencing. Another novel nanopore-based sequencing approach was proposed by Cockcroft et al. that exploited the selective, base-by-base activity of DNA Polymerase [19]. By anchoring a DNA/DNA-Polymerase complex in the nanopore, the authors were able to electrically monitor single nucleotide primer extension events. Primer extensions were controlled by providing each nucleotide set sequentially and temporally extracting sequence information [19]. The Bayley group recently demonstrated the ability to continuously resolve indigenous single nucleotides (dAMP, dCMP, dGMP, dTMP) through nanopore based resistive current measurements [18]. Remarkably, individual bases could be discriminated based on current blockade levels without any prior base labeling or chemical modification as shown in Fig. 1.2b, c. Base selectivity was achieved by modifying the mutant α-*hemolysin* pore with a cyclodextrin adapter ($am_6amPDP_1\beta CD$) covalently bound within the β barrel of the transmembrane domain, thereby constricting the nanopore channel while enhancing the chemical specificity of the sensor. Raw bases were read with over 99% confidence under optimal operating conditions. By integrating this base identification platform with a highly processive exonuclease (chemical attachment or genetic fusion of exonuclease), a single molecule sequencing by digestion approach may be feasible.

1.2.2 Bacteriophage phi29 Connector

Another biological nanopore that is receiving much interest of late is the connector protein from the bacteriophage *phi29* DNA packaging motor. In bacteriophage *phi29*, linear dsDNA is packaged into a viral capsid, an entropically unfavorable process that requires the hydrolysis of ATP. During packaging, the linear DNA passes through a narrow channel of inner diameter ~3.6 nm, termed the connector. The connector is comprised of 12 GP10 protein subunits that readily self assemble in solution to form a stable, repeatable do-decameric structure [95]. As the crystal structure of this biological nanopore channel has been resolved [100], explicit site engineering is possible. Wendell et al. modified the *phi29* connector protein to include hydrophilic sites on the crown and base, thereby allowing its integration into liposomes [95]. The insertion of the *phi29* connector into preformed lipid bilayers was achieved through vesicle fusion resulting in steady, repeatable pore conductance. Pore conductance was comparatively approximately five times higher than that observed in α-*hemolysin* under similar conditions and did not show any voltage gating effects. *Phi29* has one distinct advantage over α-*hemolysin*. The larger barrel allows the translocation of dsDNA and a variety of proteins that are simply too large to pass through α-*hemolysin*. Thus the *phi29* connector system allows the experimentalist to examine a broader spectrum of biomolecule interactions at the single molecule level. Wendell et al. demonstrated the successful detection of 5.5 kbp dsDNA and 35 bp dsDNA using this novel biological nanopore platform.

1.3 Solid-State Nanopores

With advances in microfabrication technologies, focus has shifted to the solid-state domain with numerous groups studying biomolecule transport through solid-state nanopores. Solid-state nanopores exhibit superior chemical, thermal, and mechanical stability over their biological counterparts, and can be fabricated using conventional semiconductor processes, thereby facilitating mass fabrication and size tunability. In addition, solid-state nanopores are functional over a wide range of pH and do not exhibit any voltage gating, whilst allowing for integration with electrical contacts and optical probes.

1.3.1 Fabrication of Single Nanopores

There are four primary techniques available for the fabrication of solid-state nanopores in thin Si_3N_4, SiO_2, Al_2O_3 or polymer membranes; surface tension driven oxide reflow, ion milling, track-etch method and electron beam based decompositional sputtering. Other lithography-free techniques for creating individual nanopores include focused ion beam (FIB) techniques coupled with ion-beam sculpting to achieve pore sizes as low as 10 nm [54], and laser ablation methods capable of achieving sub 100 nm pore diameters [99, 101].

1.3.1.1 Electron Beam Induced Oxide Reflow

The oxide reflow technique involves the use of e-beam lithography to pattern large 40–100 nm holes in micromachined silicon membranes. These pores are subsequently oxidized and shrunk to the sub-10 nm range using a TEM. The TEM shrinking process, discovered by Storm [84] uses a high energy electron beam to locally fluidize the oxide surface in the vicinity of the nanopore causing the oxide to reflow in the direction that minimizes interstitial surface energy. For nanopores with diameter, $d < t$, where t is the membrane thickness, nanopore shrinking was repeatedly observed. Figure 1.3 illustrates this electron beam induced shrinking process. Schenkel et al. attributed this shrinking phenomenon to the build up of a low-Z hydrocarbon layer in the nanopore during electron-beam irradiation [74]. Electron Energy Loss Spectra (EELS) from the localized nanopore region however revealed the presence of only Si and O and the absence of C, [84] thereby confirming that oxide reflow is indeed the mechanism responsible for nanopore shrinking.

The temporal contraction of a SiO_2 nanopore formed in an oxidized free standing Si membrane through electron beam induced oxide reflow processes is shown in Fig. 1.3a–d. The temporal contraction of an Al_2O_3 nanopore is illustrated in Fig. 1.3e–h [89]. The formation of SiO_2 nanopores in oxidized free standing Si membranes presents some inherent limitations. Pores were oxidized (wet oxidation)

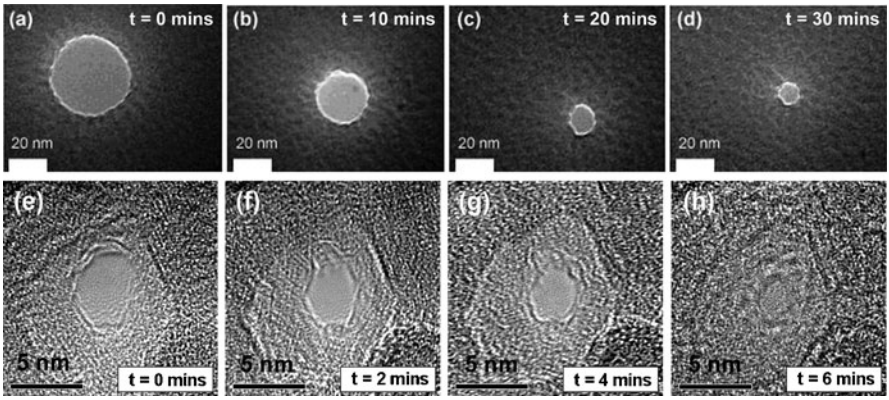

Fig. 1.3 TEM based nanopore contraction process: (**a**–**d**) Sequence of phase contrast images obtained during TEM based temporal contraction of a SiO_2 nanopore. Pore contraction was observed over a period of 30 mins from an initial pore size of ~40 nm to a final pore size of ~8 nm. (**e**–**h**) TEM based contraction of an Al_2O_3 nanopore [89], reprinted with permission. A tightly focused electron beam is used to initially sputter a pore of diameter ~4 nm. Exposure to a defocused electron beam results in material reflow into the pore, resulting in pore contraction. Final pore size is approximately 1 nm

at 900°C for 31 min resulting in a SiO_2 layer of thickness between 800 and 900 Å. This oxide layer acts as an insulating barrier, shielding the electrolyte solution from the underlying conductive Si surface. Tilted SEM images of these thermally grown silicon dioxide membranes illustrate high levels of compressive stress and membrane buckling post oxidation [89]. The result is extremely fragile, highly stressed membranes that frequently rupture during DNA translocation experiments. Fitch et al. studied the intrinsic stress and strain in thin films of SiO_2 prepared by the thermal oxidation of crystalline silicon and concluded that large intrinsic stress gradients exist in the layers of SiO_2 at the Si/SiO_2 interface [25]. The residual intrinsic interfacial stress was calculated at ~460 MPa and was independent of the growth temperature and thermal annealing processes, attributed to mismatches in the molar volumes of Si and SiO_2 at the interface. This highlights the need for low stress, mechanically stable membranes for nanopore formation.

1.3.1.2 Ion Beam Sculpting

The ion-beam sculpting process first developed by Li et al. [53], uses an energetic beam of Ar^+ ions to form nanopores with dimensions as low as 1.5 nm in thin Si_3N_4 membranes. Contrary to what one would expect, a 3 keV Ar^+ ion beam rastered continuously over a Si_3N_4 sample at room temperature resulted in ion beam assisted diffusion of atoms into the pore region resulting in nanopore contraction. The flow of matter to the developing nanopore showed temperature dependence with a transition between pore opening and pore closing consistently observed at ~5 °C under the

ion-beam conditions used. Pore expansion was attributed to ion sputter erosion at the pore edge, dominant at low temperatures and high ion flux. Pore closure was attributed to the reflow of a stressed viscous surface layer into the nanopore. The reduced viscosity and/or enhanced stress in this layer caused relaxation, thereby filling the nanopore. Feedback control was used to precisely control nanopore size.

1.3.1.3 Track-Etch Method

Conical nanopores are typically formed in μm thick polymer films using the track-etch method [10, 75, 76]. The fabrication process involves first bombarding a thin sheet of polymer material (polyethylene terephthalate, polyimide or polycarbonate) with a high energy beam of nuclear fission fragments or with a high energy ion beam from a MeV accelerator at normal or near normal incidence angle. The irradiated polymer membrane is then placed between two chambers of a conductivity cell and etched chemically from one side. Chemical-etching of the damage track is done in a strong alkaline solution (pH $\approx$ 13) with high chlorine content at elevated temperatures (~50 °C) using a solution such as sodium hypochlorite (NaOCl) [77]. The other compartment of the conductivity cell is filled with 1 M potassium iodide (KI) solution as a stopping medium for the OCl^- ions of the etchant. As soon as the etchant completely penetrates the polymer film, iodide ions reduce OCl^- to Cl^- ions thereby halting the etch process. The result is a tapered, individual conical nanopore with pore diameter as low as ~10 nm in the polymer membrane.

1.3.1.4 Electron Beam Induced Sputtering

Electron beam induced sputtering offers a rapid and reliable method to prototype *nm* sized pores in the TEM. This method involves the use of a focused convergent electron beam with sufficiently high current density to decompositionally sputter *nm* sized pores in thin oxide or nitride membranes (thickness $\leq$ 60 nm). An added benefit of this method is that it allows the operator to inspect pore size during fabrication and avoids the need for electron beam lithography involving e-beam resists and reactive ion etching (RIE) pattern transfer steps. Kim et al. used high-resolution TEM to study nanopore formation kinetics in Si_3N_4. Nanopore formation was a balance between two competing processes: (a) material sputtering and (b) surface-tension-induced shrinking [46, 48]. Nanopores, 4–8 nm in diameter were directly drilled using a JEOL 2010F field emission TEM with an accelerating voltage of 200 keV and a beam current density of 10^8–10^9 e nm^{-2}. Nanopore contraction was achieved by slightly defocusing the e-beam, effectively reducing the beam intensity to ~10^6 e nm^{-2}. TEM tomography was used to map the three-dimensional structure of these solid-state nanopores. It was observed that the sidewalls of the sputtered pores were angled (approximately 65° to the horizontal), attributed to the intensity distribution of the e-beam around its focal point. Post-drilling, pores formed an 'hourglass' structure with pore width being determined by

the width of the narrowest constriction [46–48]. Similarly, Heng et al. used a focused convergent electron beam to form nanopores in ultra-thin 10 nm Si_3N_4 membranes. The nanopore structure resembled a double cone structure with a cone angle of 10° [30]. Smeets et al. observed a cone angle of 45° for nanopores sputtered in composite SiO_2/SiN/SiO_2 membranes [81]. In all cases, nanopores formed directly through electron beam induced sputtering exhibited the ability to contract under a defocused electron beam.

1.3.2 Fabrication of Nanopore Arrays

Multiple methods exist for the formation of nanopore arrays. The track-etch method is one which has been used to produce commercially viable nanopore arrays with diameters as low as ~10 nm and packing densities as high as 6×10^8 pores/cm^2 [28]. Nanopore arrays can also be fabricated through an anodization process of thin aluminum films. In one such process that we have previously explored, aluminum foil is first anodized in a 0.3 M oxalic acid solution at 5 °C at a constant applied voltage of 40 V for 20 h [63]. The anodized aluminum is then etched in an aqueous mixture of phosphoric/chromic acid at 60 °C. Any remaining Al in the pore region is dissolved using a saturated $HgCl_2$ solution. We used this process to produce Anodized Aluminum Oxide (AAO) membranes with a highly ordered network of nanopores (diameters = 75 nm, center-to-center distance = 105 nm), as shown in Fig. 1.4a. These nanopores can be further reduced in size through atomic layer deposition (ALD). Figure 1.4b shows an array of nanopores with final diameters of 15 ± 1 nm formed using a combination of anodization and ALD processes.

Nanopore arrays can also be formed using a serial write process using ion or electron beams. Figure 1.4c, d show arrays of ~200 nm diameter nanopores with 1 μm pitch, formed in 45 ± 5 nm thick, free standing Al_2O_3 membrane using a FIB tool employing a high energy Ga^+ beam. Arrays were formed in these studies using a FEI DB235 FIB system at an accelerating potential of 30 keV and 10 pA beam current. This process can be used to achieve pore diameters as low as 30 nm by controlling the ion dose, accelerating potential and beam current. Nanopore arrays with pore sizes as low as ~20 nm have also been formed in SiO_2 using electron beam lithography processes [70]. In addition, Kim et al. demonstrated that nanopore arrays could be fabricated by stepping a focused electron probe formed in a TEM over the sample surface [47]. Though the process was time intensive, arrays with pore diameters as low as ~5 nm could be produced this way.

1.3.3 Nanopore Formation in Thin Al_2O_3 Membranes

Recently, we demonstrated the fabrication of highly sensitive, mechanically stable nanopore sensors in Al_2O_3 membranes formed via electron beam based

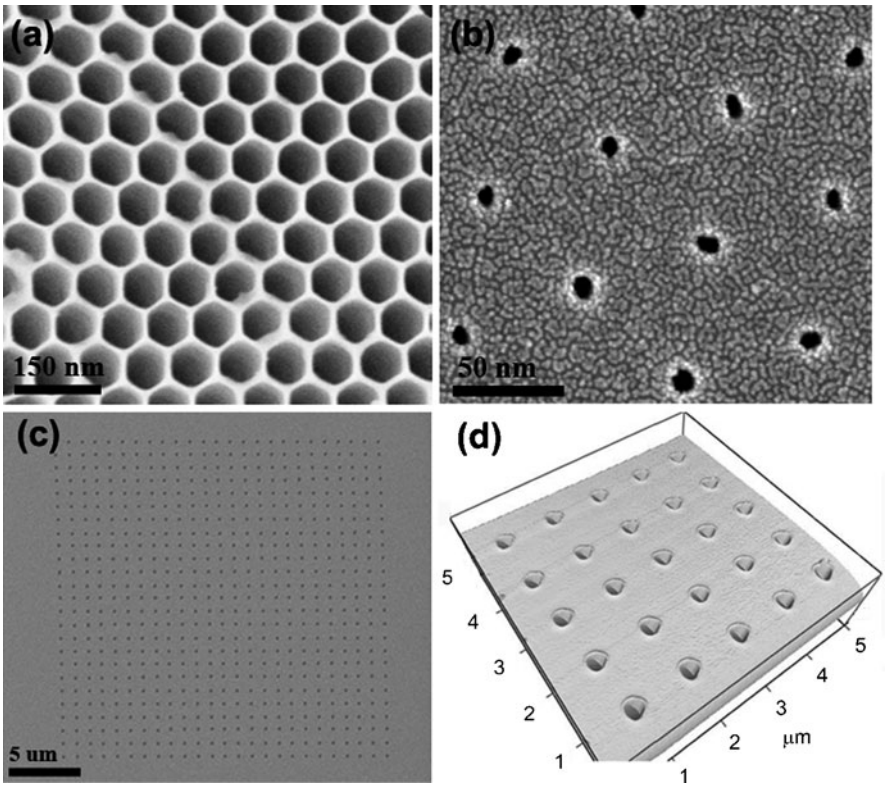

Fig. 1.4 (**a**) SEM image of an AAO nanopore array consisting of 75 nm diameter pores (**b**) SEM of AAO nanopores shrunk using the ALD process to a final pore size of 15 nm [63], reprinted with permission (**c**) SEM of nanopore array formed through FIB milling to form 200 nm pores in a 45 ± 5 nm thick free standing Al_2O_3 membrane (**d**) Atomic force microscope scan of a 5 × 5 Al_2O_3 nanopore array consisting of 200 nm nanopores, formed using the FIB tool

decompositional sputtering processes [89, 90]. Al_2O_3 membranes were formed through a combination of ALD and standard microfabrication processes resulting in low stress, 45–60 nm thick free standing membranes. In addition, these membranes were mechanically more robust than their SiO_2 counterparts as compressive thermal stress was reduced during fabrication. Nanopores formed in Al_2O_3 membranes exhibited state of the art noise performance and allowed for true VLSI device level integration due to the rapid, low temperature fabrication process developed.

1.3.3.1 Nanopore Nucleation and Expansion Kinetics

SiO_2 and various metal halides/oxides including CaF_2, AlF_3, Al_2O_3, MgO and TiO_x exhibit unique sputtering characteristics under an intense electron beam. The formation of trenches and slots in these material systems has been previously

demonstrated [3, 13, 72]. The sputtering process in Al_2O_3 is attributed to the Coulomb explosion displacement of atoms based on the Knotek-Feibelman electron-stimulated desorption mechanism. This decompositional sputtering mechanism was exploited to form nanopores ranging in diameter from 2 to 30 nm [89, 90]. Figure 1.5 shows the Gaussian/Lorentzian intensity profiles of various focused electron probes used in the pore formation process. Probe diameters of 2.3, 2.7, 3.2 and 3.9 nm full width at half maximum (FWHM) were investigated, corresponding to beam current-densities of 2.6×10^6 A/m^2, 4.2×10^6 A/m^2, 6.1×10^6 A/m^2 and 1.2×10^7 A/m^2 respectively. The inset of Fig. 1.5a is a TEM image of a 3.2 nm probe, light areas indicating regions of maximum electron intensity located at the center of the probe and darker areas indicating less intense regions located at the tail of the probe. Larger probe sizes exhibited higher peak intensities and a broader Gaussian/Lorentzian profile and were well suited to form large nanopores with diameters in the range of 10–30 nm, applicable for single molecule protein analysis and the detection of "large" analytes. Smaller probes (2.7 and 3.2 nm) exhibited lower peak intensity and a narrower profile, ideal for the high precision fabrication of 2–10 nm pores in Al_2O_3, well suited for ssDNA, dsDNA and RNA analysis.

Three stages were identified during nanopore formation in Al_2O_3, I, Pore Nucleation, II, Rapid Expansion and III, Controlled Growth as shown in Fig. 1.5b. A critical beam current density in excess of 2.6×10^6 A/m^2 was required for nanopore nucleation in Al_2O_3 membranes. This is in good agreement with threshold current densities extracted by Salisbury et al. in experiments involving electron beam sputtered anodized alumina [72]. Below this threshold, topographical damage corresponding to the cleaving of Al-O bonds (bond dissociation energy of 513 kJ/mol) [67], was observed but electron momentum was insufficient to induce an embryonic nanopore structure. Pore contraction mechanisms were also seen to dominate at low beam current densities, possibly due to surface tension driven oxide reflow, generation/recombination of closely spaced Frenkel pairs [71] and mass transport of mobile atoms into the nucleation site. This is consistent with the nanopore contraction phenomenon observed previously in SiO_2 [11, 84], and Al_2O_3 systems [89]. The sputter rate transition observed at the boundary of the Rapid Expansion and Controlled Growth stage was attributed to electron beam induced crystallization and metallization of the nanopore region.

1.3.3.2 Electron Beam Induced Crystallization

Structural phase transformations in the membrane material around the pore region was observed during electron beam induced decompositional sputtering of Al_2O_3 [89, 90]. Discrete spot reflections of α, γ, δ and κ phase Al_2O_3 were initially identified, confirming the formation of nanocrystalline clusters of preferred phases. In α-Al_2O_3, Al^{3+} cations are octahedrally coordinated with average Al-O bond lengths of 1.92 Å [6]. However, γ-Al_2O_3 typically exhibits a cubic defect-spinel type structure with average Al-O bond lengths of 1.89 Å [5]. The presence of multiple heterogeneous phases with varying bond lengths and co-ordinations,

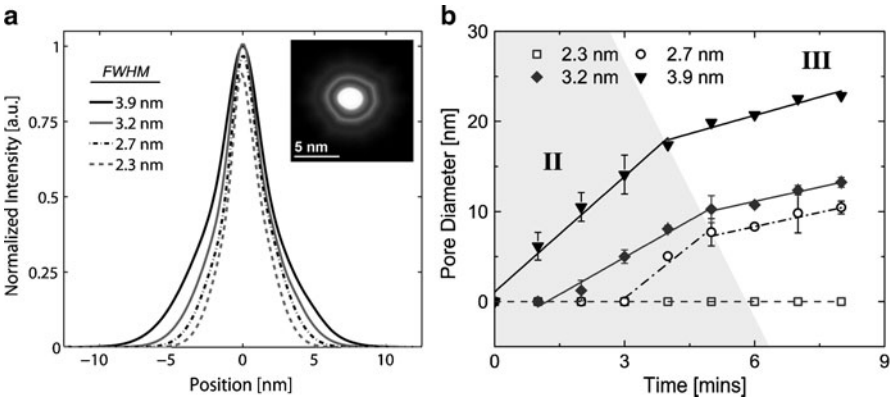

Fig. 1.5 Al_2O_3 nanopore formation kinetics [90], reprinted with permission (**a**) Intensity profiles of the focused electron probes used during nanopore formation in Al_2O_3 thin films. Intensity is normalized with respect to peak intensity of the 3.9 nm *FWHM* probe (Inset) TEM image of a 3.2 nm probe showing spatial intensity distribution (**b**) Nanopore sputtering kinetics illustrating pore diameter vs. time for the various probe sizes examined. Distinct expansion rates were observed delineating the three stages of pore formation, I Pore Nucleation (not shown), II Rapid Expansion and III Controlled Growth

confirms that an irregular density of exposed Al-O groups exists at the pore surface which in turn corresponds to an irregular surface charge distribution in a hydrated Al_2O_3 nanopore. This irregular charge distribution is expected to strongly impact DNA translocation kinetics. Prolonged exposure to the electron beam resulted in a polycrystalline structure with preferred α and/or γ phases only [90]. These results provide evidence that the surface charge in the nanopore can be engineered based on critical electron doses. Electron beam induced crystallization was not observed in Si_3N_4 and SiO_2 systems [89].

1.3.3.3 Variations in the Nanopore Stoichiometry

Wu et al. demonstrated that the electron beam inadvertently modifies the stoichiometry of the nanopore [97, 98]. Nanopores formed in ~60 nm thick SiO_2/SiN/SiO_2 membranes through electron beam sputtering, induced the formation of Si rich clusters in the vicinity of the nanopore as confirmed through electron energy loss spectroscopy (EELS) and energy filtered TEM (EFTEM). O and N were preferentially sputtered away in this case. Electron beam induced sputtering also has a dramatic impact on the composition of Al_2O_3 based nanopores. EELS analysis confirmed that Al-rich regions were formed at and near the pore edge due to the preferential desorption of O [90]. Compositional variations were calculated by the *k-factor* method [24], and revealed that the O to Al ratio in the local nanopore region decreased from 1.5 before pore formation to ~0.6 after pore formation. This result confirms that the sputtering process preferentially desorbs oxygen, leaving

behind Al-rich nanocrystals resulting in a partially metalized nanopore. Similar phenomenon has been observed in hole drilling experiments conducted in Na-β Al_2O_3 [24]. Coupled with studies by Berger et al. demonstrating the formation of continuous Al regions and "plugs" in e-beam irradiated metal β-aluminas, [3] this work provides a unique method to potentially form nano-scale metallic contacts within a nanopore for bio-sensing applications. Simulation work by Lagerqvist et al. demonstrated the ability to achieve single nucleotide resolution by employing a nanopore sensor with embedded transverse sensing electrodes, with potential application to nanopore-based DNA sequencing [50]. These results could help enable the possible realization of such a structure. Local nanopore stoichiometry is also very important when chemically modifying or functionalizing a nanopore with various biomolecules or organosilanes. The packing density of these molecules in the lumen and barrel of the nanopore are dependent on the density of Aluminol surface groups in the nanopore. Thus a thorough oxidation in an O_2 plasma is required before any surface functionalization steps.

1.3.4 Ionic Conduction Through Solid-State Nanopores

1.3.4.1 Nanopore Conductance

The conductance of the nanopore can be measured in monovalent electrolyte, typically KCl, by placing the nanopore between two electrically isolated, fluidic reservoirs. Typically, high salt solutions well in excess of physiological conditions are used (~1 M KCl, 10 mM Tris–HCl, pH 7.5) to obtain sufficiently high baseline current levels that can be monitored using a Pico ammeter. Faradaic Ag/AgCl electrodes are placed in each reservoir allowing for a localized redox based exchange reaction to occur at each electrode. After a 30 s O_2 plasma treatment, immediate wetting and ionic conduction through the nanopore is observed. Linear current-voltage characteristics are typically observed for nanopores in SiO_2, Si_3N_4 and Al_2O_3 membranes formed using TEM based decompositional sputtering processes [30, 81, 89]. The linear current-voltage characteristics of a ~11 nm pore in 1 M, 100 and 10 mM KCl electrolyte are shown in Fig. 1.6a. To further probe the performance of Al_2O_3 nanopores in electrolyte, the conductance, G, of 11 different nanopores of varying diameter (4–16 nm) were measured in 1 M KCl, as shown in Fig. 1.6b. Two geometric models were proposed to fit G [46, 48, 81]. The first model assumed a symmetric double cone structure with cone angle, α [81]. Assuming $\alpha = 30°$, [46, 48] an upper conductance bound can be derived (solid black curve of Fig. 1.6b). The second model assumed a purely cylindrical channel of length, $L_{pore} = 60$ nm with a cross sectional diameter equal to the pore diameter, d_{pore} (solid gray curve of Fig. 1.6b). This model provided a lower bound for the measured pore conductance. Applying a least squares fit to the measured data (black dashed curve of Fig. 1.6b), an effective length of $h_{eff} \approx 26.5$ nm and cone angle of $\alpha \approx 24°$ were extracted for Al_2O_3 pores formed via decompositional sputtering. The effects of surface charge were neglected in these

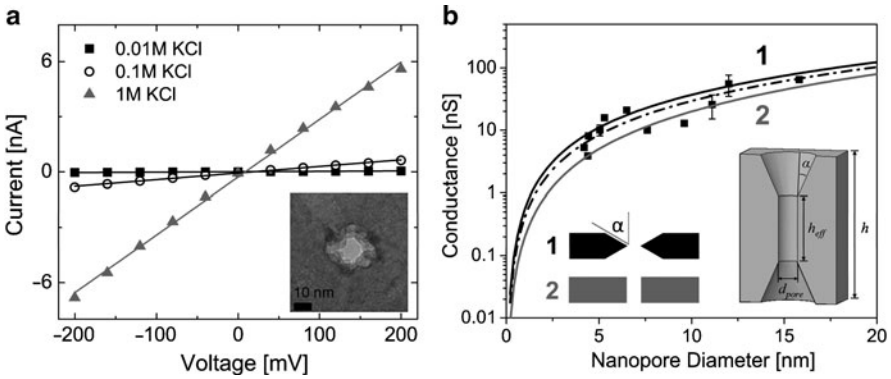

Fig. 1.6 Electrical characterization of Al_2O_3 nanopores [89], reprinted with permission. (**a**) Current-Voltage characteristics of a 11 nm diameter pore measured in 10 mM KCl, 100 mM KCl and 1 M KCl. Linear current-voltage characteristics suggest pore geometry is symmetric in the *z*-direction (**b**) Pore conductance of 11 nanopores ranging in diameter from 4 to 16 nm. Black and gray solid lines represent conductance models for geometries 1 (double cone) and 2 (cylindrical), shown in the inset. Black dashed line is a least squares fit to the measured data, used to extract pore parameters $h_{eff} \approx 26.5$ nm and $\alpha \approx 24°$. (Right Inset) Predicted cylindrical, double cone geometry of an Al_2O_3 pore from conductance measurements and energy filtered TEM imaging

models as the Debye screening length given by κ^{-1} (where $K^2 = 2e^2 n_{KCL}/k_B T\varepsilon\varepsilon_0$ in 1 M KCl) $<< d_{pore}$. At these high salt concentrations, charge carriers in the bulk were expected to dominate current flow. Electro osmotic flows resulting from counterion condensation on the charged pore surface should be negligible. These results confirmed that a symmetric, double cone nanopore structure was formed through decompositional sputtering. TEM tomograms taken by Wu et al. and Kim et al. on SiO_2/SiN/SiO_2 and Si_3N_4 nanopores further confirmed the double cone, symmetric structure of a TEM sputtered solid-state nanopore [46, 48, 98].

Asymmetric current-voltage characteristics have been reported in synthetic nanopores formed in polyethylene terephthalate (PET) polymer membranes [76, 78]. The track etch method used to form these nanopores produced an asymmetric, conical geometry resulting in a structure that significantly rectifies the ionic current. This conically shaped, highly charged nanopore is cation selective, exhibiting diode like behavior in fluid with a preferential direction for the cation flow from the narrow entrance toward the wide opening of the pore. Siwy et al. further demonstrated some of the novel characteristics of this architecture by pumping ions against a concentration gradient using a fluctuating electric force applied across the membrane in the form of an AC voltage signal [76].

1.3.4.2 Surface Charge Effects

The effects of surface charge on pore conductance were investigated by Ho et al. using nanopores formed in 10 nm thick Si_3N_4 membranes [33]. At low electrolyte

concentrations ($\leq$10 mM), pore conductivity was found to be much larger than bulk approximations calculated using pore geometry. This conductance deviation was attributed to Debye layer overlap in the pore (Debye length is comparable to or larger than the pore radius). Multiscale simulations of ion transport through these pores coupled with experimental results suggested the presence of fixed negative charges on the pore wall, and a reduction of the ion mobility due to fixed charge and ion proximity to the pore wall.

Consistent with Ho's results, Smeets et al. [81] found that in ~10 nm diameter SiO_2 pores, the negative surface charge lining the pore walls dominates pore conductivity at salt concentration below ~0.1 M. Interestingly, a variable surface charge density in the pore was extracted as a function of electrolyte concentration in these experiments. pH dependent studies performed by Wanunu et al. in Si_3N_4 nanopores did not reveal any significant changes in the conductance with varying pH [93]. Nanopores formed in PET membranes also exhibited a net negatively charged surface at neutral and slightly basic pH's due to the deprotonation of carboxylate groups on the pore walls. The average density of carboxylate groups was estimated to be 1.5 groups/nm^2 [78]. In contrast to SiO_2, TiO_2 only presented a slightly negatively charged surface at neutral or slightly basic pH. Unlike the variable surface charge observed by Smeets et al. in SiO_2 pores, TiO_2 nanopore conductance saturated at very low electrolyte concentrations [65, 68]. Nam et al. extracted a surface charge density of ~0.005 mC/m^2 in TiO_2 pores, significantly lower than the charge density observed in SiO_2 pores which is estimated at between ~25 and 50 mC/m^2 [65]. Nam suggested that this low charge density may be responsible for the saturation in ionic conductivity at lower KCl concentrations than expected.

In contrast to the aforementioned systems, Al_2O_3 nanopores are expected to be positively charged at neutral or slightly basic pH. The formation of hetero-phase crystalline domains (in particular γ and α-phases) of varying bond lengths and co-ordinations during electron beam irradiation impart a non-uniform charge density in the pore. α-Al_2O_3 and γ-Al_2O_3 both exhibit different points-of-zero-charge (pzc's), estimated at pH 9.1 and pH 8.5 in monovalent salt solution [1, 88]. In addition, the Zeta potentials of these materials measured in pH 7.5 electrolyte are ~50 mV and ~25 mV respectively, [7, 27] and thus these charged nanocrystalline domains are expected to interact with ions and charged polymers in the pore differently [90].

1.3.4.3 Manipulating Surface Charge in Nanopores

As mentioned, precise control over phase transformations in Al_2O_3 nanopore systems by varying electron dose provides a novel method to engineer surface charge at the nanopore/fluid interface via the electron beam. This is very interesting from a materials perspective. Another approach for tuning surface charge in the nanopore is through electrical mechanisms. Nam et al. embedded a TiN gate electrode directly in the nanopore and showed current rectification by applying potentials to the gate electrode [65]. This gating behavior was only observed at very

low salt concentrations ($<10^{-3}$ M) where the effects of surface charge are dominant and Debye layer overlap in the nanopore is indeed expected. P-type unipolar behavior was observed suggesting that K^+ ions are the majority carriers in these TiO_2 gated nanopores. Studies by Kalman et al. focused on integrating a Au electrode into a conical nanopore [42]. By modulating the electric potential applied to the gate, one alters the distribution of ions in the overlapping Debye layer in the pore and thus the potential distribution in the pore. Using this approach Kalman et al. were able to manipulate the current through the device from the rectifying behavior synonymous with conical nanopores to a near linear type behavior as seen in structurally symmetric nanopores. The mechanism for this change in transport behavior was accredited to the enhancement of concentration polarization induced by the gate. The manipulation of surface charge through the chemical modification of solid-state nanopores will be discussed in subsequent sections.

1.3.5 Noise in Solid-State Nanopores

Electrical noise in ionic current measurements involving solid-state nanopores limits the utility of these systems in wide spread nucleic acid based diagnostics. Two dominant sources of noise have been documented in the literature; a low frequency current fluctuation with $1/f$ characteristics (flicker noise) and a high-frequency background noise component associated with the relatively high capacitance of the insulating membrane on the support chip (dielectric noise) [16, 35, 79, 80, 82, 86, 87]. Minimizing these respective noise components is integral to improving the sensitivity and signal to noise ratio of nanopore sensors.

1.3.5.1 1/*f* Noise in Solid-State Nanopores

$1/f$ noise has been observed in many physical and biological systems. $1/f$ noise is present in the form of fluctuations in the voltages or currents of semiconductors, the voltage across nerve membranes and synthetic membranes and in the resistance of aqueous ionic solutions [45]. The power spectrum, denoted by $S(f)$, is proportional to the reciprocal of the frequency in a narrow bandwidth as illustrated in eq. 1.1.

$$S(f) = \frac{constant}{|f|^{\alpha}} \qquad where\ 0 < \alpha < 2 \tag{1.1}$$

Hoogerheide et al. studied the $1/f$ noise characteristics of Si_3N_4 nanopores as a function of pH and electrolyte ionic strength and concluded that $1/f$ noise originates from surface charge fluctuations at the nanopore surface [35]. The model presented was based on protonization of surface functional groups and was sensitive to as few as tens of active surface groups in the nanopore. In contrast, Smeets et al. concluded that low frequency noise was predominantly due to the number of charge carriers

in the nanopore thereby following Hooge's phenomenological relation rather than on the surface charge fluctuations and composition of the nanopore surface [79, 80, 82]. Surface modifications however have been shown to significantly improve the 1/*f* noise characteristics of nanopores. Chen et al. used an atomic layer deposition process to coat Si_3N_4 nanopores with Al_2O_3 and saw significant reductions in 1/*f* noise [14, 15]. Tabard-Cossa et al. demonstrated a significant reduction in 1/*f* noise by treating nanopore chips with piranha solution [86]. It is therefore likely that 1/*f* noise in nanopores is a combination of the two mechanisms described previously; that is, fluctuations in the total number of charge carriers in the nanopore coupled with a fluctuation in their mobilities due to trapping at surface sites. As expected, 1/*f* noise was observed in our experiments involving nanopores sputtered in Al_2O_3 thin films and were comparable in magnitude to noise levels observed in biological nanopores. By addressing the surface properties of solid-state nanopores, through either chemical surface treatment or material choice, improved noise performance may be achieved.

1.3.5.2 Dielectric Noise

Dielectric noise in nanopores is associated with the capacitance of the nanopore chip and scales linearly with frequency. Nanopores are typically fabricated in dielectric thin film such as SiO_2 or Si_3N_4, anchored on a conductive Si substrate. These dielectric materials are typically lossy and have a dissipation factor, D, associated with them. Smeets et al. extracted a dissipation factor of 0.27 ± 0.07 for Si_3N_4 pores, strongly deviating from $D = 0$ for an ideal capacitor [80, 82]. The dielectric noise can be reduced by minimizing the capacitance of the substrate. To achieve this, the thickness of the Si substrate can be increased or the fluidic contact area on the chip can be minimized. Tabard-Cossa et al. selectively patterned PDMS on Si_3N_4 chips to reduce the fluidic contact area and thereby minimized dielectric noise [86].

Using various micro-fabrication processes and PDMS fluidic isolation techniques, we achieved noise performance that surpasses the state-of-the-art in Si_3N_4 technology as reported by Tabard-Cossa et al. [86]. Noise reduction was attributed to a decrease in device capacitance, measured at 20 ± 5 pF [89] as compared to device capacitance in Si_3N_4 structures, which was measured in excess of 300 pF [80, 82]. Noise performance was further optimized using the three structures illustrated in Fig. 1.7. Architecture 1 consisted of 45 ± 5 nm thick Al_2O_3 membranes formed on a low resistivity Si substrate. Architecture 2 consisted of a 500 nm thick SiN passivation layer added on top of the Al_2O_3 layer with a 30 μm square opening forming the membrane region. PDMS gaskets with 300 μm openings were bonded to the chip to further decrease device capacitance. Architecture 3 consisted of a ~1.5 μm thick SiN passivation layer added on top of the Al_2O_3 layer with a 5 μm circular opening containing the Al_2O_3 membrane area. This stack was formed on a high resistivity Si wafer ($\rho = 10{,}000$ Ω-cm), effective in reducing leakage currents through the substrate. PDMS gaskets containing a 300 μm opening

were bonded to the front side of the nanopore chip. These structures helped us incrementally reduce device capacitance and thereby reduce dielectric noise. Impedance spectra (magnitude and phase) were obtained for each architecture as shown in Fig. 1.7d, e, and fitted to an equivalent RC circuit. A capacitance of 1 nF, 300 pF and 20 pF was extracted for architectures 1, 2 and 3 respectively, corresponding to peak-to-peak noise values of approximately 1.2 nA, 400 pA and 200 pA at the 100 kHz bandwidth setting on the Axopatch 200B measurement platform, as shown in Fig. 1.7f. Capacitance minimization has proven to be an effective method in decreasing high frequency dielectric noise, improving signal-to-noise ratio and enhancing the overall sensitivity of these nanopore sensors in DNA translocation experiments.

1.3.6 DNA Translocation Through Solid-State Nanopores

The first demonstrations of DNA translocation through a solid-state nanopore were shown by Li et al. [53]. Deep current blockades were observed as dsDNA was electrophoretically driven through nanopores formed in thin Si_3N_4 membranes using the ion beam sculpting process described earlier. Further studies confirmed the dependence of dsDNA transport kinetics on bias voltage, DNA length and DNA conformation [52]. Li et al. further showed that by reducing the bias voltage by a factor of two, the dwell time of the DNA molecule in the nanopore could be approximately doubled [52]. Multiple configurations of the translocating molecule in the nanopore were also observed in these experiments attributed to dsDNA folding, a phenomenon observed primarily in large nanopores. Smaller ~3 nm pores however, were shown to restrict the passage of folded molecules and promoted only the linear passage of unfolded molecules. Heng et al. demonstrated that by reducing nanopore diameter to below that of dsDNA, the electrophoretic separation of ssDNA from dsDNA could be achieved using a solid-state nanopore [29]. Narrow ~2 nm pores were seen to block the passage of dsDNA and allowed the passage of only ssDNA. Only by applying very high fields was dsDNA permeation through these narrow pores indeed possible attributed to stretching transitions that occur in dsDNA at forces exceeding 60 pN. Comer et al. further demonstrated that very narrow $<$1.6 nm diameter synthetic nanopores could be effectively used to unzip hairpin DNA [20]. Different modes of hairpin DNA transport were observed in these experiments, the first mode referring to the unzipping of the double helix structure to form ssDNA and the second mode referring to the stretching/distortion of the double helix itself.

Chang et al. studied the effect of buffer concentration on DNA translocation dynamics [11]. Current enhancements were observed in large SiO_2 nanopores at low salt concentrations (100 mM KCl) as opposed to the typical blockades that were observed at higher salt concentrations. A more rigorous study by Smeets et al. and Chang et al. suggested that these current enhancements are due to counterion condensation on the DNA backbone, thereby locally increasing the concentration of

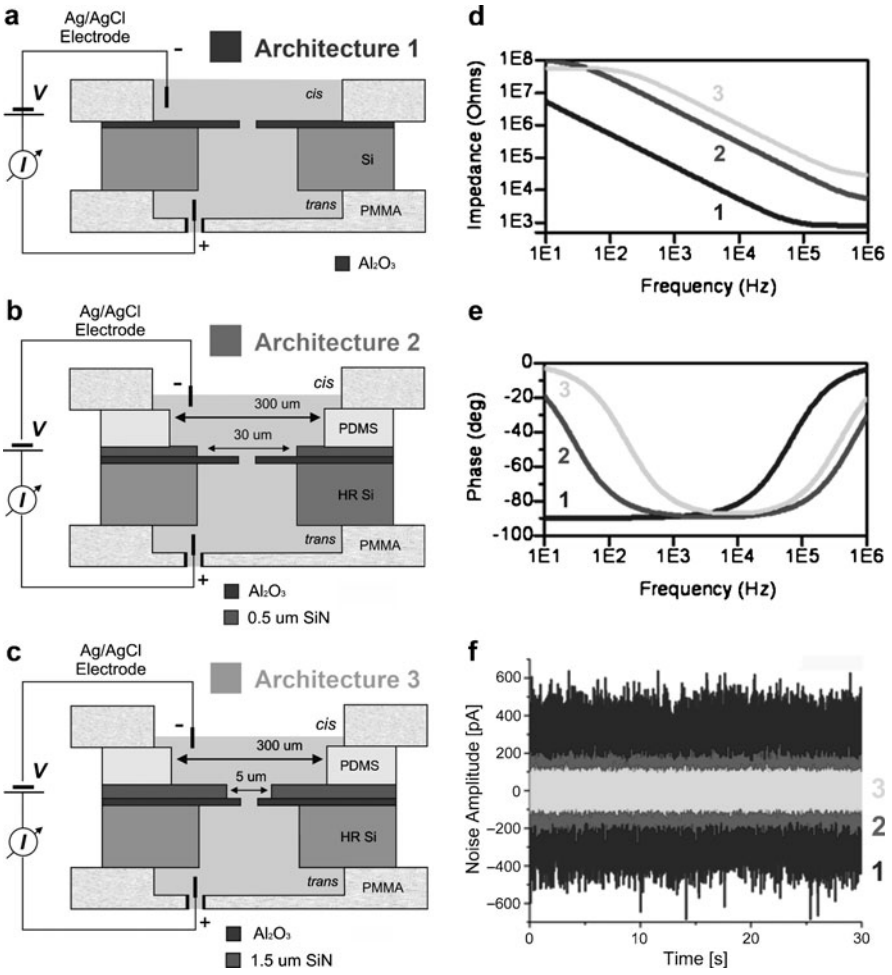

Fig. 1.7 Dielectric noise reduction in solid-state Al_2O_3 nanopores (**a**) Architecture 1 consists of a 45 ± 5 nm thick Al_2O_3 membranes formed on a low resistivity Si substrate. (**b**) Architecture 2 consists of a 500 nm thick SiN passivation layer added on top of the Al_2O_3 film with a 30 μm square opening forming the membrane region. PDMS gaskets with 300 μm openings were bonded to the chip to further decrease device capacitance. (**c**) Architecture 3 consists of a 1.5 μm thick SiN passivation layer added on top of the Al_2O_3 film with a patterned 5 μm circular opening constituting the Al_2O_3 membrane area. This stack was formed on a high resistivity Si wafer ($\rho = 10{,}000\Omega$-cm) (**d** and **e**) Impedance magnitude and phase spectra for the various architectures investigated. By fitting to an equivalent RC circuit, capacitances of 1 nF, 300 pF and 20 pF were extracted for architectures 1, 2 and 3 respectively (**f**) Normalized current traces in 1 M KCl, 10 mM Tris, pH 7.5 buffer at an applied voltage of 200 mV for architectures 1, 2 and 3. Capacitance reduction decreases the peak-to-peak noise from 1.2 nA (architecture 1), to 400 pA (architecture 2), to 200 pA (architecture 3)

counterions in the pore during DNA transport [12, 81]. Current enhancements were observed at concentrations below 0.4 M, a phenomenon that seems localized to only large SiO_2 nanopores. Distinct current blockades were observed in 100 mM salt solution during the transport of λ-DNA through 2.2 nm SiN nanopores [23]. In biological *α-hemolysin*, Benner et al. demonstrated that current blockades were still observed at low salt concentrations (300 mM KCl) during the entry of dsDNA into the lumen of the pore [2]. Current blockades were also observed during the transport of dsDNA through Al_2O_3 nanopores in 100 mM KCl salt [90].

Polymer velocity in the nanopore is also a key topic of interest. Translocation velocities of up to ~30 bases/μs have been reported at relatively low bias voltages in Si_3N_4 nanopores [26]. Chen et al. observed similar translocation velocities in large Al_2O_3 coated Si_3N_4 nanopores estimated at ~27 bases/μs [14, 15]. Such high translocation velocities limit the utility of conventional nanopore technologies in high end DNA sensing and analysis applications including single nucleotide detection. Fologea et al. demonstrated that by increasing electrolyte viscosity using glycerol and by decreasing temperature and bias voltage, an order of magnitude reduction in translocation velocity could be achieved [26]. Remarkably, even with these improvements, the translocation velocities through a solid-state nanopore are still more than an order of magnitude faster than that observed in biological *α-hemolysin* [14, 15]. Lubensky accredited the slow translocation rates in *α-hemolysin* to strong polymer interactions with the pore walls [56]. High translocation velocities were also observed in large ~10 nm SiO_2 nanopores [85]. Despite these high velocities, Storm et al. showed that it is indeed possible to size long dsDNA using solid-state nanopores, in a rapid and label free manner [85]. In contrast to bulk gel-electrophoresis methods, length separation using solid-state nanopores allows each molecule to be screened and interrogated individually.

The kinetics of DNA transport through solid-state nanopores is also of interest from a polymer physics stand point. Translocation kinetics suggests that the majority of events in larger nanopores are fast translocation events, where the dwell time, t_D, is significantly less than the characteristic relaxation time or *Zimm* time [85]. The *Zimm* time, t_Z, is an upper bound on the time taken by a polymer to reach an entropically and sterically favored state. For events where $t_D < t_Z$, the molecule was said to exhibit a *frozen* polymer configuration during transport, hindered by only the hydrodynamic drag on the part of the molecule outside the pore [85]. The effects of specific polymer-pore interactions were not accounted for in these studies. Wanunu et al. discussed the importance of surface interactions on dsDNA transport through Si_3N_4 nanopores [94]. Studies performed using small 2.7–5 nm pores revealed an order of magnitude increase in dwell times as pore diameter was decreased from 5 to 2.7 nm. In addition, strong temperature dependence was observed confirming that surface interactions play an important role in polymer transport. Surface interactions were also seen to play an important role in the transport of dsDNA through small ~5 nm Al_2O_3 nanopores [89]. These interactions were characterized by a monoexponential decay in dwell time histograms with time constants consistent with timescales observed in Si_3N_4 systems [89].

1.3.6.1 Surface Enhanced DNA Transport Through Al_2O_3 Nanopores

More and more evidence is emerging supporting the notion that nanopore surface interactions play an integral role in determining the dynamics of DNA transport. Nanopore surface characteristics including stoichiometry, morphology, surface charge density, charge polarity, cone angle and *rms* roughness are all expected to factor into this argument. In fact, we recently reported that surface interactions can help enhance the detection capabilities of solid-state nanopore sensors [90]. In experiments involving the electrophoretic transport of 5 kbp dsDNA through 7 nm diameter nanocrystalline Al_2O_3 nanopores, mean dwell-times at 100 mV yielded a translocation velocity of ~1.4 nucleotides/μs, more than an order of magnitude slower than dsDNA transport through Si_3N_4 nanopores (~30 nucleotides/μs) at similar biases [26], but an order of magnitude faster than single stranded DNA translocation through α-hemolysin [14, 15].

Figure 1.8 illustrates the voltage dependent transport of dsDNA through a 7 nm nanocrystalline Al_2O_3 nanopore. Two distinct timescales are observed in the translocation time histograms of Fig. 1.8, summarized in Fig. 1.8d [90]. The shorter timescale exhibited strong voltage dependence and was associated with fast polymer transport through the nanopore with minimal DNA-nanopore interactions. Such fast translocations are indeed probable in large 7 nm pores via translocation through the central pore region where the effects of surface binding sites and surface charge are significantly screened. Fast translocation events were not observed in smaller ~5 nm Al_2O_3 nanopores suggesting that pore size and Debye layer thickness indeed play an important role in regulating the velocity of DNA transport [89]. The longer timescale observed was associated with DNA translocations involving significant interactions with the nanopore. The origins of these interactions are hydrophobic and/or electrostatic in nature and are dependent partially on the material properties of the pore (stoichiometry, morphology and surface roughness). As previously discussed, materials analysis confirmed the formation of hetero-phase crystalline domains (in particular γ and α phase Al_2O_3) of varying bond lengths and coordinations in the nanopore region, resulting in non-uniform distributions of exposed Al-O groups at the pore surface. In a hydrated nanopore, these surface sites react with adsorbed water to form protonated hydroxyl groups at pH 7.5, resulting in a net positive, non-homogeneous surface charge density across the pore. These positively charged nanocrystalline domains are expected to interact strongly with anionic DNA. In fact, modeling results by Kejian et al. confirmed that polymer translocation velocities in a solid-state nanopore are heavily dependent on zeta potential and surface charge [44]. Alterations to pore stoichiometry due to the preferential desorption of O and the aggregation of Al is also expected to result in a distribution of equilibrium constants (pK's) for the protonizable chemical sites across the pore. The resulting electrostatic interactions/binding between the non-homogeneous, net positively charged nanopore surface and anionic DNA is one factor contributing to the *slow* translocation velocities observed in experiments involving Al_2O_3 nanopores. This strong electrostatic binding was not reported in SiO_2 and Si_3N_4, likely as these systems exhibit a net

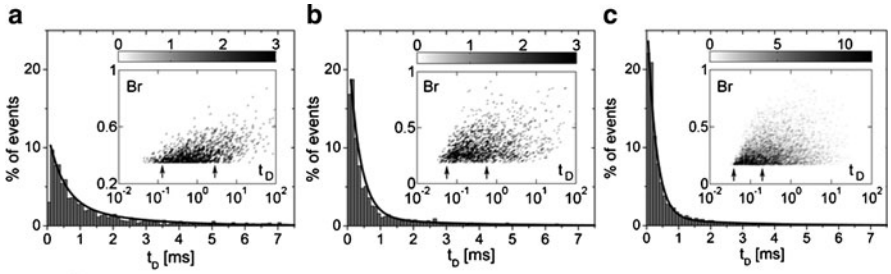

d

Voltage	100 mV	300 mV	500 mV
I (Open Pore) [nA]	0.23	0.7	1.2
$\mu(t_D)$ [ms]	3.5 ± 10.8	1.3 ± 4.3	0.8 ± 1.9
t_1 [ms]	0.48 ± 0.05	0.35 ± 0.01	0.28 ± 0.02
t_2 [ms]	2.0 ± 0.7	2.9 ± 1.3	2.6 ± 2.2
$\mu(B_r)$ [%]	0.42	0.32	0.28
n [events]	1421	1954	5351
R [Hz]	4.7	6.5	17.9

Fig. 1.8 Dwell time histograms for the transport of 5 kbp dsDNA through a 7 nm nanocrystalline Al_2O_3 nanopore in 100 mM KCl, 10 mM Tris, pH 7.5 buffer at applied voltages of (**a**) 100 mV (**b**) 300 mV and (**c**) 500 mV [90], reprinted with permission. Each distribution is fitted with a bi-exponential function (*black line*) with two time constants, t_1 and t_2, indicating two distinct types of polymer transport, fast translocation governed by polymer hydrodynamics and slow translocation regulated by polymer-pore interactions. (Insets) Blockage Ratio (B_r) vs. Dwell time (t_D) [ms] event density plots at each voltage. Grayscale bar represents number of events. At higher voltages, a greater percentage of events exhibit fast translocation dynamics bounded by the arrows in the insets. Translocation events exhibit clear voltage dependence (**d**) Summary of results from the electrical sensing of 5 kbp dsDNA through 7 nm Al_2O_3 nanopores. t_D Dwell time (time biomolecule resides in the pore); t_1 Time constant corresponding to fast translocation; t_2 Time constant corresponding to slow translocation; B_r Blockage Ratio (percentage of open pore current that is blocked during DNA translocation); n Biomolecule Flux (total number of events during 5 min of recording); R Capture Rate (average number of translocation events per second)

negatively charged surface at pH 7.5 resulting from the deprotonation of surface silanol groups [35]. Furthermore, a comparison of the surface charge density of Si_3N_4 and γ-Al_2O_3 surfaces at pH 7.5 (in monovalent salt solution at concentration 1×10^{-4} M) revealed a charge density that is approximately six times higher in γ-Al_2O_3 (50 mC/m^2) than in Si_3N_4 (8 mC/m^2) systems [1, 81]. Thus, polymer-pore interactions involving electrostatic binding events are expected to be more pronounced in Al_2O_3 nanopores.

The importance of polymer-pore interactions are explored further in the following section through nanopore based chemical modification. Chemical modification and surface functionalization of nanopores has helped usher in the next generation of nanopore sensors relying on polymer-pore interactions to achieve selective and facilitated transport of various biomolecules through individual nanopores and nanopore arrays.

1.3.7 Chemically Modified Solid-State Nanopore Sensors

Chemical modification of the surface of solid-state nanopores offers a method to tailor the physical and chemical properties of the nanopore. Selective transport through functionalized solid-state nanopore arrays was previously demonstrated by varying nanopore size (thereby restricting biomolecule passage based on molecular weight) [38], nanopore surface charge [17], and nanopore polarity [39] (to achieve the selective transport of either hydrophobic or hydrophilic molecules). More recently, focus has shifted to the attachment of specific recognition sequences or tethered receptors in the nanopore for target specific molecular recognition. In drug screening and medicine, such a technique provides a means for label-free, real-time kinetic analysis of biomolecular interactions at the single molecule level including protein-protein, protein-DNA and receptor-ligand interactions. In fact, Lee et al. demonstrated that enantiomeric drug separations could be achieved using an antibody functionalized nanoporous array [51]. Functionalized nanopore channels can also help elucidate the mechanisms driving biological processes, including cell signaling and regulation. Jovanovic-Talisman demonstrated that functionalized polycarbonate nanoporous arrays can reproduce the selectivity of nuclear pore complexes (NPCs), an essential component in the trafficking of specific macromolecules between the cell nucleus and cytoplasm [41]. Proteins referred to as phenylalanine-glycine (FG)-nucleoporins typically line the walls of NPCs and facilitate the transient binding and passing of transport factors and their cargo-bound complexes, while restricting the passage of proteins that fail to specifically bind to FG-nucleoporins [69]. Using nanopore channels of the correct dimensions coated with FG-nucleoporins, Jovanovic-Talisman et al. were able to reproduce key features of nucleocytoplasmic transport, selectively discriminating against control proteins in favor of transport factors and transport factor cargo complexes. Kohli demonstrated that selective permeation through synthetic nanoporous membranes could be achieved using DNA hybridization as the selective transport mechanism [49]. In this specific example, a gold nanoporous array was functionalized using hairpin DNA with a thiol substituent at the 5′ end allowing it to be covalently attached to the inside walls of the array. The analyte of interest was 18 base long ssDNA which was either a perfect complement to the loop of the hairpin or contained a single base mismatch. Using optical absorbance methods, Kohli demonstrated that single nucleotide polymorphisms could be detected using this chemically modified nanopore platform under optimal conditions.

Various strategies have been implemented to chemically modify solid-state nanopores. Covalent attachment chemistries are generally preferred due to the stability and high packing density of self assembled monolayers (SAM's) on well prepared sufaces. A very common SAM preparation involves the reaction of molecules with a sulfhydrl termination group (−SH) with Au surfaces to form S-Au attachments to the surface. An extensive review on the formation of SAM's on Au surfaces of varying curvatures is provided by Love et al. [55]. In many cases however, the surface of the nanopore may be an insulating oxide or nitride (SiO_2, Si_3N_4, Al_2O_3). In these cases a covalent attachment chemistry specific to this

insulating surface is required. Liquid phase silane based chemistries are the most commonly used technique to functionalize individual nanopores in such insulating membranes [66, 93]. While these surface chemistries have been characterized in detail on planar surfaces, questions still remain as to the exact packing density, molecular orientation and thickness of SAM's in a highly confined environment that is a nanopore. In addition, nanopores formed via TEM decompositional sputtering processes typically exhibit high surface roughness, high surface curvature and a non-stoichiometric material composition due to selective material sputtering as observed in SiO_2 coated Si_3N_4 nanopores [97, 98], further complicating the nanopore functionalization process. In these cases it is vital to thoroughly oxidize the surface through an extensive O_2 plasma treatment or a liquid based treatment in 1:3 H_2O_2:H_2SO_4. Using such a process, Wanunu et al. showed a change in the pH response of Si_3N_4 nanopore functionalized with various amine terminated silane chemistries in comparison to non-functionalized Si_3N_4 nanopores [93]. Ionic conductance measurements were used to monitor in-situ the formation of the SAM in the nanopore and to calculate the thickness of the molecular layer directly attached to the internal surface of the nanopore. The calculated values suggested the upright orientation of the attached molecules on the nanopore surface. Note, in this specific example, the entire membrane containing the nanopore was functionalized with the silane chemistry.

For certain applications however, it may be desirable to functionalize only the nanopore region itself. For example, in applications where the analyte of interest is present only at very low concentrations, a functionalized membrane may reduce the detection limits of the nanopore due to delocalized binding events on the membrane surface between immobilized receptors and the target species, without yielding detectable changes in the output signal [37]. In addition, receptors immobilized on the membrane may themselves modulate the conductance of the nanopore, even in the absence of the target species. Hofler et al. showed via coarse-grained molecular dynamics simulations that DNA anchored on the membrane surface can electrically gate the nanopore if bound sufficiently close to the pore opening [34]. A localized nanopore functionalization process was explored by Nilsson et al. and involved the localized deposition of a tetraethylorthosilicate (TEOS) based oxide ring around the nanopore [66]. A focused ion beam was used to decompose the TEOS precursor near the Si nanopore surface, thereby reducing the diameter of the pore to a final diameter of between 25 and 30 nm. DNA probes were immobilized in the nanopore via a silane based chemistry thereby introducing local chemical functionality at the entrance of the nanopore without functionalizing the remainder of the Si membrane. SAM coatings may also help to reduce the speed of polymer translocation through nanopores. Kim et al. derivatized Al_2O_3 nanopore surfaces with aminopropyltriethoxysilane (APTES) resulting in a positively charged surface in pH 6.0 buffer, attractive to anionic dsDNA [46, 48]. The resulting strong electrostatic polymer-pore interactions enabled the detection of short dsDNA molecules that are typically under the detection limits of conventional solid-state nanopore sensors. In addition to SAM coatings, highly functional lipid bilayer coatings on nanopores are also possible [91], permitting the potential integration with sensitive biological nanopore channels.

Perhaps the most striking example of nanopore functionalization impacting the sensing capabilities of single nanopore channels involves the use of oxidized Si nanopores functionalized with hairpin-loop, probe DNAs to selectively transport short "target" (complementary) ssDNAs under an applied electrical field [36]. Iqbal et al. functionalized SiO_2 nanopores with 20 base long hairpin-loop DNA probes containing a 6 bp stem forming region. Mismatches were introduced in the target ssDNA at points complementary to the stem forming region of the immobilized probes. Higher flux and smaller translocation times were observed during the passage of Perfectly Complementary (PC) DNA as opposed to single base mismatch (1MM) DNA. This was attributed to an attractive potential between the immobilized probe and the target PC-DNA resulting in hairpin unzipping and facilitated transport of the PC sequence. In the case of 1MM however, a repulsive potential was proposed between the target sequence and the probe resulting in probe-target interaction without unzipping of the hairpin. Reduced biomolecule flux and increased translocation times were also consistently observed in the cases of two and three base mismatch DNAs (2MM and 3MM respectively) relative to PC-DNA. These studies confirm that it is indeed possible to impart chemical selectivity in single solid-state nanopores and this selectivity can be electrically monitored through translocation signatures at the single-molecule level. Such devices could help further unravel the physics of selective and facilitated transport of biomolecules through nanoscale channels and could play an important role in medical diagnostics.

1.4 Conclusions

Solid-state nanopore sensors are highly versatile platforms for the rapid, label-free detection and analysis of single molecules, with potential application to next generation DNA sequencing. The versatility of this technology allows for both interfacing with biological systems at the nano-scale as well as large scale VLSI integration promising reliable, affordable, mass producible biosensors with single molecule sensing capabilities. This technology may also serve as a base to provide further insight into the mechanisms driving biological processes, including cell signaling and regulation through gated, selective ion channels, protein secretion across cellular membranes and viral infection by phages. The applications for solid-state nanopore technology are diverse. Point-of-care diagnostic devices employing solid-state nanopores can be used to detect and monitor infectious diseases e.g. influenza, an effective tool in public health strategies. In defense, solid-state nanopores can be used for the rapid detection of high priority agents such as Bacillus anthracis (anthrax) at very low concentrations. In drug screening and medical applications, solid-state nanopores provide a means for label-free, real-time kinetic analysis of biomolecular interactions at the single molecule level including protein-protein, protein-DNA and receptor-ligand interactions. This technology finds broad application in bio-nanotechnology.

Acknowledgments We thank the staff at *Micro and Nanotechnology Lab and Frederick Seitz Materials Research Lab*, University of Illinois at Urbana-Champaign for their assistance. We acknowledge the funding from the National Institutes of Health through the NIH Roadmap for Medical Research Nanomedicine Development Center (PN2 EY 018230) and NIH R21 EB007472.

References

1. Alami-Younssi, S., Larbot, A., Persin, M., Sarrazin, J., & Cot, L. (1995). Rejection of mineral salts on a gamma alumina nanofiltration membrane Application to environmental process. *Journal of Membrane Science, 102*, 123–129.
2. Benner, Seico, Chen, Roger J. A., Wilson, Noah A., Abu-Shumays, Robin, Hurt, Nicholas, Lieberman, Kate R., et al. (2007). Sequence-specific detection of individual DNA polymerase complexes in real time using a nanopore. *Nat Nano, 2*(11), 718–724.
3. Berger, S. D., Salisbury, I. G., Milne, R. H., Imeson, D., & Humphreys, C. J. (1987). Electron energy-loss spectroscopy studies of nanometre-scale structures in alumina produced by intense electron-beam irradiation. *Philosophical Magazine Part B, 55*(3), 341–358.
4. Bhakdi, S., & Tranum-Jensen, J. (1991). Alpha-toxin of Staphylococcus aureus. *Microbiol. Mol. Biol. Rev., 55*(4), 733–751.
5. Bouchet, Danièle, & Colliex, Christian (2003). Experimental study of ELNES at grain boundaries in alumina: intergranular radiation damage effects on Al-L23 and O-K edges. *Ultramicroscopy, 96*(2), 139–152.
6. Bourdillon, A. J., El-mashri, S. M., & Forty, A. J. (1984). Application of TEM extended electron energy loss fine structure to the study of aluminium oxide films. *Philosophical Magazine A, 49*(3), 341–352.
7. Bowen, Paul, Carry, Claude, Luxembourg, David, & Hofmann, Heinrich (2005). Colloidal processing and sintering of nanosized transition aluminas. *Powder Technology, 157*(1–3), 100–107.
8. Brun, L., Pastoriza-Gallego, M., Oukhaled, G., Mathe, J., Bacri, L., Auvray, L., et al. (2008). Dynamics of polyelectrolyte transport through a protein channel as a function of applied voltage. *Physical Review Letters, 100*(15).
9. Cantor, C. R., & Schimmel, P. R. (1980). *Biophysical Chemistry, Part II: Techniques for the Study of Biological Structure and Function*. New York: W.H. Freeman.
10. Chad Harrell, C., Siwy, Z. S., & Martin, C. R. (2006). Conical Nanopore Membranes: Controlling the Nanopore Shape13. *Small, 2*(2), 194–198.
11. Chang, H., Kosari, F., Andreadakis, G., Alam, M. A., Vasmatzis, G., & Bashir, R. (2004). DNA-Mediated Fluctuations in Ionic Current through Silicon Oxide Nanopore Channels. *Nano Lett., 4*(8), 1551–1556.
12. Chang, H., Venkatesan, B. M., Iqbal, S., Andreadakis, G., Kosari, F., Vasmatzis, G., et al. (2006). DNA counterion current and saturation examined by a MEMS-based solid state nanopore sensor. *Biomedical Microdevices, 8*(3), 263–269.
13. Chen, G. S., Boothroyd, C. B., & Humphreys, C. J. (1998). Electron-beam-induced damage in amorphous SiO2 and the direct fabrication of silicon nanostructures. *Philosophical Magazine A, 78*, 491–506.
14. Chen, P., Gu, J., Brandin, E., Kim, Y. R., Wang, Q., & Branton, D. (2004). Probing Single DNA Molecule Transport Using Fabricated Nanopores. *Nano Letters, 4*(11), 2293–2298.
15. Chen, P., Mitsui, T., Farmer, D.B., Golovchenko, J., Gordon, R.G., & Branton, D. (2004). Atomic Layer Deposition to Fine-Tune the Surface Properties and Diameters of Fabricated Nanopores. *Nano Lett., 4*(7), 1333–1337.
16. Chen, Peng, & Gillis, Kevin D. (2000). The Noise of Membrane Capacitance Measurements in the Whole-Cell Recording Configuration. *Biophysical Journal, 79*(4), 2162–2170.

17. Chun, Kyoung-Yong, & Stroeve, Pieter (2002). Protein Transport in Nanoporous Membranes Modified with Self-Assembled Monolayers of Functionalized Thiols. *Langmuir, 18*(12), 4653–4658.
18. Clarke, J., Wu, H. C., Jayasinghe, L., Patel, A., Reid, S., & Bayley, H. (2009). Continuous base identification for single-molecule nanopore DNA sequencing. *Nature Nanotechnology, 4*(4), 265–270.
19. Cockroft, Scott L., Chu, John, Amorin, Manuel, & Ghadiri, M. Reza (2008). A Single-Molecule Nanopore Device Detects DNA Polymerase Activity with Single-Nucleotide Resolution. *Journal of the American Chemical Society, 130*(3), 818–820.
20. Comer, J., Dimitrov, V., Zhao, Q., Timp, G., & Aksimentiev, A. (2009). Microscopic mechanics of hairpin DNA translocation through synthetic nanopores. *Biophys J, 96*(2), 593–608.
21. Coulter, W. H. (1953). Means for counting particles suspended in a fluid, United States Patent 2656508.
22. Dekker, Cees (2007). Solid-state nanopores. *Nat Nano, 2*(4), 209–215.
23. Dimitrov, V., Mirsaidov, U., Mansfield, W., Miner, J., Klemens, F., Cirelli, R., et al. (2009). Nanopores in solid-state membranes engineered for single molecule detection. *Nanotechnology, 21*(6), 065502.
24. Egerton, R. F. (1996). *Electron Energy-Loss Spectroscopy in the Electron Microscope* (Second Edition ed.). New York: Plenum Press.
25. Fitch, J. T., Bjorkman, C. H., Lucovsky, G., Pollak, F. H., & Yin, X. (1989). *Intrinsic stress and stress gradients at the SiO_2/Si interface in structures prepared by thermal oxidation of Si and subjected to rapid thermal annealing*. Paper presented at the Proceedings of the 16th annual conference on the physics and chemistry of semiconductor interfaces, Bozeman, Montana, USA.
26. Fologea, Daniel, Uplinger, James, Thomas, Brian, McNabb, David S., & Li, Jiali (2005). Slowing DNA Translocation in a Solid-State Nanopore. *Nano Letters, 5*(9), 1734–1737.
27. Franks, George V., & Meagher, Laurence (2003). The isoelectric points of sapphire crystals and alpha-alumina powder. *Colloids and Surfaces A: Physicochemical and Engineering Aspects, 214*(1–3), 99–110.
28. Gyurcsányi, R. E. (2008). Chemically-modified nanopores for sensing. *TrAC Trends in Analytical Chemistry, 27*(7), 627–639.
29. Heng, J. B., Aksimentiev, A., Ho, C., Marks, P., Grinkova, Y. V., Sligar, S., et al. (2006). The electromechanics of DNA in a synthetic nanopore. *Biophysical Journal, 90*(3), 1098–1106.
30. Heng, J. B., Ho, C., Kim, T., Timp, R., Aksimentiev, A., Grinkova, Y. V., et al. (2004). Sizing DNA Using a Nanometer-Diameter Pore. *Biophys. J., 87*(4), 2905–2911.
31. Heng, J. B., Aksimentiev, A., Ho, C., Marks, P., Grinkova, Y.V., Sligar, S., et al. (2005). Stretching DNA Using the Electric Field in a Synthetic Nanopore. *Nano Lett., 5*(10), 1883–1888.
32. Henrickson, Sarah E., Misakian, Martin, Robertson, Baldwin, & Kasianowicz, John J. (2000). Driven DNA Transport into an Asymmetric Nanometer-Scale Pore. *Physical Review Letters, 85*(14), 3057.
33. Ho, Chuen, Qiao, Rui, Heng, Jiunn B., Chatterjee, Aveek, Timp, Rolf J., Aluru, Narayana R., et al. (2005). Electrolytic transport through a synthetic nanometer-diameter pore. *Proceedings of the National Academy of Sciences of the United States of America, 102*(30), 10445–10450.
34. Höfler, Lajos, & Gyurcsányi, Róbert E. (2008). Coarse Grained Molecular Dynamics Simulation of Electromechanically-Gated DNA Modified Conical Nanopores. *Electroanalysis, 20*(3), 301–307.
35. Hoogerheide, D. P., Garaj, S., & Golovchenko, J. A. (2009). Probing Surface Charge Fluctuations with Solid-State Nanopores. *Physical Review Letters, 102*(25).

36. Iqbal, Samir M., Akin, Demir, & Bashir, Rashid (2007). Solid-state nanopore channels with DNA selectivity. *Nat Nano, 2*(4), 243–248.
37. Jagerszki, Gyula, Gyurcsanyi, Robert E., Hofler, Lajos, & Pretsch, Erno (2007). Hybridization-Modulated Ion Fluxes through Peptide-Nucleic-Acid- Functionalized Gold Nanotubes. A New Approach to Quantitative Label-Free DNA Analysis. *Nano Letters, 7* (6), 1609–1612.
38. Jirage, Kshama B., Hulteen, John C., & Martin, Charles R. (1997). Nanotubule-Based Molecular-Filtration Membranes. *Science, 278*(5338), 655–658.
39. Jirage, Kshama B., Hulteen, John C., & Martin, Charles R. (1999). Effect of Thiol Chemisorption on the Transport Properties of Gold Nanotubule Membranes. *Analytical Chemistry, 71*(21), 4913–4918.
40. Jonas, D., Walev, I., Berger, T., Liebetrau, M., Palmer, M., & Bhakdi, S. (1994). Novel path to apoptosis: small transmembrane pores created by staphylococcal alpha-toxin in T lymphocytes evoke internucleosomal DNA degradation. *Infect. Immun., 62*(4), 1304–1312.
41. Jovanovic-Talisman, T., Tetenbaum-Novatt, J., McKenney, A. S., Zilman, A., Peters, R., Rout, M. P., et al. (2009). Artificial nanopores that mimic the transport selectivity of the nuclear pore complex. *Nature, 457*(7232), 1023–1027.
42. Kalman, Eric B., Sudre, Olivier, & Siwy, Zuzanna S. (2009). Control of Ionic Transport through an Ionic Transistor based on Gated Single Conical Nanopores. *Biophysical Journal, 96*(3, Supplement 1), 648a-648a.
43. Kasianowicz, J. J., Brandin, E., Branton, D., & Deamer, D. W. (1996). Characterization of individual polynucleotide molecules using a membrane channel. *Proc. Natl Acad. Sci. USA, 93*(24), 13770.
44. Kejian, Ding, Weimin, Sun, Haiyan, Zhang, Xianglei, Peng, & Honggang, Hu (2009). Dependence of zeta potential on polyelectrolyte moving through a solid-state nanopore. *Applied Physics Letters, 94*(1), 014101–014103.
45. Keshner, M. S. (1982). 1/f noise. *Proceedings of the IEEE, 70*(3), 212–218.
46. Kim, M. J., McNally, B., Murata, K., & Meller, A. (2007). Characteristics of solid-state nanometre pores fabricated using a transmission electron microscope. *Nanotechnology 20*, 205302
47. Kim, M. J., Wanunu, M., Bell, D. C., & A. Meller (2006). Rapid Fabrication of Uniformly Sized Nanopores and Nanopore Arrays for Parallel DNA Analysis. *Advanced Materials, 18*(23), 3149–3153.
48. Kim, Y. R., Min, J., Lee, I. H., Kim, S., Kim, A. G., Kim, K., et al. (2007). Nanopore sensor for fast label-free detection of short double-stranded DNAs. *Biosensors and Bioelectronics, 22*(12), 2926–2931.
49. Kohli, Punit, Harrell, C. Chad, Cao, Zehui, Gasparac, Rahela, Tan, Weihong, & Martin, Charles R. (2004). DNA-Functionalized Nanotube Membranes with Single-Base Mismatch Selectivity. *Science, 305*(5686), 984–986.
50. Lagerqvist, Johan, Zwolak, Michael, & Di Ventra, Massimiliano (2006). Fast DNA Sequencing via Transverse Electronic Transport. *Nano Letters, 6*(4), 779–782.
51. Lee, Sang Bok, Mitchell, David T., Trofin, Lacramioara, Nevanen, Tarja K., Soderlund, Hans, & Martin, Charles R. (2002). Antibody-Based Bio-Nanotube Membranes for Enantiomeric Drug Separations. *Science, 296*(5576), 2198–2200.
52. Li, Jiali, Gershow, Marc, Stein, Derek, Brandin, Eric, & Golovchenko, J. A. (2003). DNA molecules and configurations in a solid-state nanopore microscope. *Nat Mater, 2*(9), 611–615.
53. Li, Jiali, Stein, Derek, McMullan, Ciaran, Branton, Daniel, Aziz, Michael J., & Golovchenko, Jene A. (2001). Ion-beam sculpting at nanometre length scales. *Nature, 412*(6843), 166–169.
54. Lo, Chih Jen, Aref, Thomas, & Bezryadin, Alexey (2006). Fabrication of symmetric sub-5 nm nanopores using focused ion and electron beams. *Nanotechnology, 17*(13), 3264–3267.
55. Love, J. Christopher, Estroff, Lara A., Kriebel, Jennah K., Nuzzo, Ralph G., & Whitesides, George M. (2005). Self-Assembled Monolayers of Thiolates on Metals as a Form of Nanotechnology. *Chemical Reviews, 105*(4), 1103–1170.

56. Lubensky, D. K., & Nelson, D. R. (1999). Driven Polymer Translocation Through a Narrow Pore. *Biophysical Journal, 77*(4), 1824–1838.
57. Manning, G. S. (1993). A Condensed Counterion Theory for Polarization of Polyelectrolyte Solutions in High Fields. *Journal of Chemical Physics, 99*(1), 477–486.
58. Mathe, Jerome, Aksimentiev, Aleksei, Nelson, David R., Schulten, Klaus, & Meller, Amit (2005). Orientation discrimination of single-stranded DNA inside the α-hemolysin membrane channel. *Proceedings of the National Academy of Sciences of the United States of America, 102*(35), 12377–12382.
59. McNally, Ben, Wanunu, Meni, & Meller, Amit (2008). Electromechanical Unzipping of Individual DNA Molecules Using Synthetic Sub-2 nm Pores. *Nano Lett*.
60. Meller, A., & Branton, D. (2002). Single molecule measurements of DNA transport through a nanopore. *Electrophoresis, 23*(16), 2583–2591.
61. Meller, A., Nivon, L., & Branton, D. (2001). Voltage-Driven DNA Translocations through a Nanopore. *Physical Review Letters, 86*(15), 3435.
62. Mitchell, Nick, & Howorka, Stefan (2008). Chemical Tags Facilitate the Sensing of Individual DNA Strands with Nanopores13. *Angewandte Chemie International Edition, 47*(30), 5565–5568.
63. Moon, Jeong-Mi, Akin, Demir, Xuan, Yi, Ye, Peide, Guo, Peixuan, & Bashir, Rashid (2009). Capture and alignment of *phi29* viral particles in sub-40 nanometer porous alumina membranes. *Biomedical Microdevices, 11*(1), 135–142.
64. Nakane, J., Akeson, M., & Marziali, A. (2002). Evaluation of nanopores as candidates for electronic analyte detection. *Electrophoresis, 23*(16), 2592–2601.
65. Nam, Sung-Wook, Rooks, Michael J., Kim, Ki-Bum, & Rossnagel, Stephen M. (2009). Ionic Field Effect Transistors with Sub-10 nm Multiple Nanopores. *Nano Letters, 9*(5), 2044–2048.
66. Nilsson, J., Lee, J. R. I., Ratto, T. V., & Létant, S. E. (2006). Localized Functionalization of Single Nanopores. *Advanced Materials, 18*(4), 427–431.
67. O'Keeffe, M., & Stuart, J. A. (2002). Bond energies in solid oxides. *Inorganic Chemistry, 22*(1), 177–179.
68. Parks, George A. (2002). The Isoelectric Points of Solid Oxides, Solid Hydroxides, and Aqueous Hydroxo Complex Systems. *Chemical Reviews, 65*(2), 177–198.
69. Peters, Reiner (2005). Translocation Through the Nuclear Pore Complex: Selectivity and Speed by Reduction-of-Dimensionality. *Traffic, 6*(5), 421–427.
70. Petrossian, L., Wilk, S. J., Joshi, P., Hihath, S., Goodnick, S. M., & Thornton, T. J. (2007). Fabrication of Cylindrical Nanopores and Nanopore Arrays in Silicon-On-Insulator Substrates. *Journal of Microelectromechanical Systems, 16*(6), 1419–1428.
71. Pivin, Jean Claude (1983). An overview of ion sputtering physics and practical implications. *Journal of Materials Science, 18*(5), 1267–1290.
72. Salisbury, I. G., Timsit, R. S., Berger, S. D., & Humphreys, C. J. (1984). Nanometer scale electron beam lithography in inorganic materials. *Applied Physics Letters, 45*(12), 1289–1291.
73. Sanger, F., Nicklen, S., & Coulson, A. R. (1977). DNA sequencing with chain-terminating inhibitors. *Proceedings of the National Academy of Sciences of the United States of America, 74*(12), 5463–5467.
74. Schenkel, T., Radmilovic, V., Stach, E. A., Park, S. J., & Persaud, A. (2003). Formation of a few nanometer wide holes in membranes with a dual beam focused ion beam system. *Journal of Vacuum Science & Technology B: Microelectronics and Nanometer Structures, 21*(6), 2720–2723.
75. Siwy, Z., Dobrev, D., Neumann, R., Trautmann, C., & Voss, K. (2003). Electro-responsive asymmetric nanopores in polyimide with stable ion-current signal. *Applied Physics A: Materials Science & Processing, 76*(5), 781–785.
76. Siwy, Z., & Fulinski, A. (2004). A nanodevice for rectification and pumping ions. *American Journal of Physics, 72*(5), 567–574.

77. Siwy, Z., Heins, E., Harrell, C. Chad, Kohli, P., & Martin, C.R. (2004). Conical-Nanotube Ion-Current Rectifiers: The Role of Surface Charge. *Journal of the American Chemical Society, 126*(35), 10850–10851.
78. Siwy, Z. S. (2006). Ion-Current Rectification in Nanopores and Nanotubes with Broken Symmetry. *Advanced Functional Materials, 16*(6), 735–746.
79. Smeets, R. M. M., Dekker, N. H., & Dekker, C. (2009). Low-frequency noise in solid-state nanopores. *Nanotechnology, 20*(9), 095501.
80. Smeets, R. M. M., Keyser, U. F., Dekker, N. H., & Dekker, C. (2008). Noise in solid-state nanopores. *Proceedings of the National Academy of Sciences, 105*(2), 417–421.
81. Smeets, R. M. M., Keyser, U. F., Krapf, D., Wu, M. Y., Dekker, N. H., & Dekker, C. (2006). Salt Dependence of Ion Transport and DNA Translocation through Solid-State Nanopores. *Nano Lett., 6*(1), 89–95.
82. Smeets, R. M. M., Kowalczyk, S. W., Hall, A. R., Dekker, N. H., & Dekker, C. (2008). Translocation of RecA-Coated Double-Stranded DNA through Solid-State Nanopores. *Nano Letters*.
83. Stoddart, David, Heron, Andrew J., Mikhailova, Ellina, Maglia, Giovanni, & Bayley, Hagan (2009). Single-nucleotide discrimination in immobilized DNA oligonucleotides with a biological nanopore. *Proceedings of the National Academy of Sciences, 106*(19), 7702–7707.
84. Storm, A. J., Chen, J. H., Ling, X. S., Zandbergen, H. W., & Dekker, C. (2003). Fabrication of solid-state nanopores with single-nanometre precision. *Nat Mater, 2*(8), 537–540.
85. Storm, A. J., Storm, C., Chen, J., Zandbergen, H., Joanny, J.-F., & Dekker, C. (2005). Fast DNA Translocation through a Solid-State Nanopore. *Nano Lett., 5*(7), 1193–1197.
86. Tabard-Cossa, Vincent, Trivedi, Dhruti, Wiggin, Matthew, Jetha, Nahid N., & Marziali, Andre (2007). Noise analysis and reduction in solid-state nanopores. *Nanotechnology, 18*(30), 305505.
87. Uram, Jeffrey D., Ke, Kevin, & Mayer, Michael (2008). Noise and Bandwidth of Current Recordings from Submicrometer Pores and Nanopores. *ACS Nano, 2*(5), 857–872.
88. Veeramasuneni, S., Yalamanchili, M. R., & Miller, J. D. (1996). Measurement of Interaction Forces between Silica and [alpha]-Alumina by Atomic Force Microscopy. *Journal of Colloid and Interface Science, 184*(2), 594–600.
89. Venkatesan, B. M., Dorvel, B., Yemenicioglu, S., Watkins, N., Petrov, I., & Bashir, R. (2009). Highly Sensitive, Mechanically Stable Nanopore Sensors for DNA Analysis. *Advanced Materials, 21*(27), 2771–2776.
90. Venkatesan, B. M., Shah, A. B., Zuo, J. M., & Bashir, R. (2010). DNA Sensing Using Nanocrystalline Surface-Enhanced Al_2O_3 Nanopore Sensors. *Advanced Functional Materials, 20*(8), 1266–1275.
91. Venkatesan, B. M., Polans, J., Comer, J., Sridhar, S., Wendell, D., Aksimentiev, A., & Bashir, R. (2011). Lipid Bilayer Coated Al_2O_3 Nanopore Sensors: Towards a Hybrid Biological Solid-State Nanopore. *Biomedical Microdevices*, DOI: 10.1007/s10544-011-9537-3.
92. Vercoutere, Wenonah, Winters-Hilt, Stephen, Olsen, Hugh, Deamer, David, Haussler, David, & Akeson, Mark (2001). Rapid discrimination among individual DNA hairpin molecules at single-nucleotide resolution using an ion channel. *Nat Biotech, 19*(3), 248–252.
93. Wanunu, Meni, & Meller, Amit (2007). Chemically Modified Solid-State Nanopores. *Nano Letters, 7*(6), 1580–1585.
94. Wanunu, Meni, Sutin, Jason, McNally, Ben, Chow, Andrew, & Meller, Amit (2008). DNA Translocation Governed by Interactions with Solid State Nanopores. *Biophys. J.*, biophysj.108.140475.
95. Wendell, David, Jing, Peng, Geng, Jia, Subramaniam, Varuni, Lee, Tae Jin, Montemagno, Carlo, et al. (2009). Translocation of double-stranded DNA through membrane-adapted phi29 motor protein nanopores. *Nat Nano, 4*(11), 765–772.
96. Winters-Hilt, Stephen (2007). The alpha-Hemolysin nanopore transduction detector - single-molecule binding studies and immunological screening of antibodies and aptamers. *BMC Bioinformatics, 8*(Suppl 7), S9.

97. Wu, M. Y., Krapf, D., Zandbergen, M., Zandbergen, H. W., & Batson, P. E. (2005). Formation of nanopores in a SiN/SiO_2 membrane with an electron beam. *Applied Physics Letters, 87*(11), 113106–113103.
98. Wu, M. Y., Smeets, R. M. M., Zandbergen, M., Ziese, U., Krapf, D., Batson, P. E., et al. (2009). Control of Shape and Material Composition of Solid-State Nanopores. *Nano Letters, 9*(1), 479–484.
99. Wu, Shanshan, Park, Sang Ryul, & Ling, Xinsheng Sean (2006). Lithography-Free Formation of Nanopores in Plastic Membranes Using Laser Heating. *Nano Letters, 6*(11), 2571–2576.
100. Xiang, Ye, Morais, Marc C., Battisti, Anthony J., Grimes, Shelley, Jardine, Paul J., Anderson, Dwight L., et al. (2006). Structural changes of bacteriophage [phi]29 upon DNA packaging and release. *EMBO J, 25*(21), 5229–5239.
101. Yu, Minrui, Kim, Hyun-Seok, & Blick, Robert H. (2009). Laser drilling of nano-pores in sandwiched thin glass membranes. *Opt. Express, 17*(12), 10044–10049.